Journal of Thermal Analysis and Calorimetry
https://doi.org/10.1007/s10973-024-13568-9

Martensitic transformations and magnetic properties of $Ni_{50-x}Mn_{37}Sn_{13}Fe_x$($x = 0.5, 1, 1.5$) melt-spun ribbons

W. Younsi[1,2] · S. Louidi[3,4] · J. J. Suñol [5] · A. Bouaine[6] · J. Daza[5]

Received: 12 September 2023 / Accepted: 3 August 2024

Abstract
The present study investigates the influence of iron (Fe) doping on the martensitic transformation and magnetic properties of $Ni_{50-x}Mn_{37}Sn_{13}Fe_x$($x = 0.5, 1, 1.5$) magnetic shape memory alloys in ribbon form. The ribbons were prepared using arc-melting followed by melt-spinning processes and were characterized using X-ray diffraction, scanning electron microscopy, differential scanning calorimetry, and vibrating sample magnetometry. Our findings demonstrate that the addition of Fe shifts the martensitic transformation to lower temperatures and increases the Curie point of the austenitic phase, T_c^A, leading to an enhanced magnetism in the austenitic phase. Moreover, a significant increase in the magnetization jump (ΔM) is observed, from 3.3 emu g^{-1} for $x = 1$ to 17 emu g^{-1} for $x = 1.5$ under a 50 Oe applied magnetic field. The structural transformations are also found to be sensitive to the external applied magnetic field. The isothermal magnetization curves exhibit the exchange bias effect, which confirms the coexistence of antiferromagnetic and ferromagnetic coupling in the samples. Furthermore, the exchange bias effect increases with the Fe content.

Keywords Ferromagnetic shape memory alloys · Melt-spun ribbons · Martensitic phase transformation · Exchange bias effect

Introduction

Non-stoichiometric NiMn-X (X=Sn, In, Ga, and Sb) ferromagnetic shape memory alloys have attracted considerable attention in recent years due to their multifunctional properties, such as Exchange Bias (EB) [1–3], memory shape effect [4], magnetocaloric effect [5, 6], magnetoresistance [7, 8], and elastocaloric effect [9]. These alloys undergo a first-order reversible martensitic transformation from the ferromagnetic cubic austenite phase to the weak magnetic martensitic phase with lower symmetry (tetragonal, modulated monoclinic, or orthorhombic) upon cooling. This magneto-structural transition is associated with an abrupt change in magnetization, which affects the magnetic entropy change (ΔS_M) [5]. Due to these interesting properties, these alloys are potential candidates for magnetic refrigeration devices, sensors, and actuation devices [10, 11]. The magnetism in these alloys is mainly attributed to the Mn magnetic

✉ J. J. Suñol
joanjosep.sunyol@udg.edu

W. Younsi
w.younsi@univ-skikda.dz

S. Louidi
s.louidi@univ-skikda.dz

A. Bouaine
bouaine_abdelhamid@univ-jijel.dz

J. Daza
jason.daza@cadscrits.udg.edu

[1] Laboratoire Physique de la Matière Condensée et Nanomatériaux (LPMCN), Faculté des Sciences Exactes et Informatique, Université de Jijel, 18000 Jijel, Algeria

[2] Département de Technologie, Faculté de Technologie, Université 20 Août 1955-Skikda, 21000 Skikda, Algeria

[3] Département de Physique, Faculté des Sciences, Université 20 Août 1955-Skikda, 21000 Skikda, Algeria

[4] Laboratoire de Magnétisme et de Spectroscopie des Solides LM2S, Faculté des Sciences, Université Badji-MokhtarAnnaba, B.P 12, 23000 Annaba, Algeria

[5] Departament De Fisica, Universitat de Girona, 17071 Girona, Spain

[6] Département de Physique, Faculté des Sciences Exactes et Informatique, Université de Jijel, 18000 Jijel, Algeria

Published online: 09 September 2024

moment, and their magnetic properties strongly depend on the Mn-Mn inter-atomic distances, which are relatively large, resulting in indirect exchange interactions via the conduction electrons [12, 13]. The transformation temperatures and magnetic properties are highly sensitive to the chemical composition of the alloy and fourth-element doping. Transition metal doping, such as with Fe and Co, has been found to be highly effective in tuning the transformation temperatures and enhancing the magnetic properties [14–16]. Previous researches have indicated that replacement of Mn or Ni by Fe or Co can enhance the magnetic properties and tune the transformation temperatures of these alloys [15–18]. In Mn-rich Heusler $Mn_{50}Ni_{41}In_9$ ribbon materials, substituting Mn with 1 $at\%$ Fe caused both martensitic and magnetic transition temperatures to decrease by about 33 K. Increasing Fe content to 2 $at\%$ resulted in a slight increase in the two transitions and a large overlap. Further increasing Fe to 3% caused the magnetic transition in the austenite phase to vanish [19]. Ghosh and Mandal [20] investigated Mn-rich Mn-Ni-Fe-Sn Heusler alloys by substituting Fe for Ni and Mn. They found that replacing Ni with Fe decreased the martensitic transition temperature, but substitution of Mn with Fe increased this temperature. They also observed a large magnetic entropy change and high refrigerant capacities with a small percentage of Fe doping (2 $at\%$). In recent studies, substitution of Ni with 1.1 $at\%$ of Fe in $Ni_{50}Mn_{38}Sn_{12}$ alloy resulted in a magnetization jump ΔM of 36.7 $A\,m^2\,kg^{-1}$, almost twice as large as that in the undoped alloy (19.7 $A\,m^2\,kg^{-1}$) [21]. In $Ni_{42}Mn_{49}Sn_9$ alloy, replacing Ni with Fe enhanced the magnetization, reaching a maximum value of 49 $A\,m^2\,kg^{-1}$ for 4 $at\%$ Fe, and decreasing the martensitic transformation temperature [15]. The addition of Co or Fe as the fourth element in Ni-Mn-Sn based alloys can lead to the precipitation of the γ phase [15, 22–24], which causes chemical composition segregation and adversely affects the magneto-structural properties [25]. However, the fast kinetics of crystallization associated with melt spinning can suppress the formation of the γ phase [26]. Moreover, melt spinning facilitates the fabrication of textured samples with enhanced mechanical properties. The specific geometry of the resulting ribbons offers distinct advantages for the development of magnetocaloric materials, as it facilitates efficient heat exchange with the heat transfer fluid within a magnetocaloric device, enabling rapid thermal transfer [27, 28]. From a technological standpoint, the use of melt spinning is attractive because it obviates the need for expensive heat treatment stages. Fe or Co has been added as a fourth element in several studies involving Ni-Mn-Sn-based ribbons [18, 29–32]. In the present work, we perform a systematic investigation of the effect of Fe doping and applied magnetic field on the martensitic transformation and magnetic properties of $Ni_{50-x}Mn_{37}Sn_{13}Fe_x (x = 0.5,\ 1,\ 1.5)$ melt-spun ribbons.

Experimental

Non-stoichiometric $Ni_{50-x}Mn_{37}Sn_{13}Fe_x (x = 0.5,\ 1,\ 1.5)$ Heusler alloys were synthesized by arc melting high purity elements ($> 99.9\,at\%$) under an argon atmosphere. To ensure homogeneity, the constituent elements were melted four times. The obtained ingots were then induction-melted in a quartz tube in a melt-spinning system, and ejected into an argon environment onto the polished surface of a copper wheel rotating at a linear speed of 48 $m\,s^{-1}$. The microstructural morphology and chemical composition of the resulting melt-spun ribbons were examined using a scanning electron microscope (*SEM*) equipped with an X-ray energy dispersive spectroscopy (*EDS*) microanalysis system. The melt-spinning technique offers advantages for ribbon production, including compositional homogeneity and a polycrystalline texture with a small grain size, which can facilitate martensitic phase nucleation [33]. The structure and properties of the ribbons depend on several factors, including the velocity of the rotating wheel and ejection conditions [34]. To ensure consistency, all samples in this work were produced using the same melt-spinning conditions. The crystallographic structure of the ribbons at room temperature was determined using X-ray diffraction (*XRD*) with $CuK\alpha$ radiation ($\lambda = 0.154060\,nm$), a step size of $2\theta = 0.02°$, and a counting time of 15 s. The *XRD* patterns were analyzed using the *MAUD* program [35] based on the Rietveld method [36]. The austenite-martensite structural transformations were studied using differential scanning calorimetry (*DSC*). Cyclic experiments were performed under a liquid nitrogen atmosphere with a cooling and heating rate of 10 $K\,min^{-1}$ to determine the thermal characteristics of the ribbons. Thermomagnetic measurements were conducted using a vibrating sample magnetometer (*VSM-VersaLab, QD*) with zero-field-cooling (*ZFC*), field-cooling (*FC*), and field-heating (*FH*) protocols over a temperature range of 50 K to 400 K and an applied magnetic field up to 50 kOe.

Results and discussions

Microstructure

Figure 1 shows typical *SEM* micrographs of the free surface [(a), (b) and (c)] and the fracture cross section [(d), (e) and (f)] of $Ni_{50-x}Mn_{37}Sn_{13}Fe_x (x = 0.5,\ 1,\ 1.5)$ Heusler alloys ribbons. The free surface of the ribbons exhibits a granular microstructure, characterized by nearly equiaxed grains. Additionally, a distinct twin-variants relief of the martensitic substructure is clearly observed for $x = 0.5$

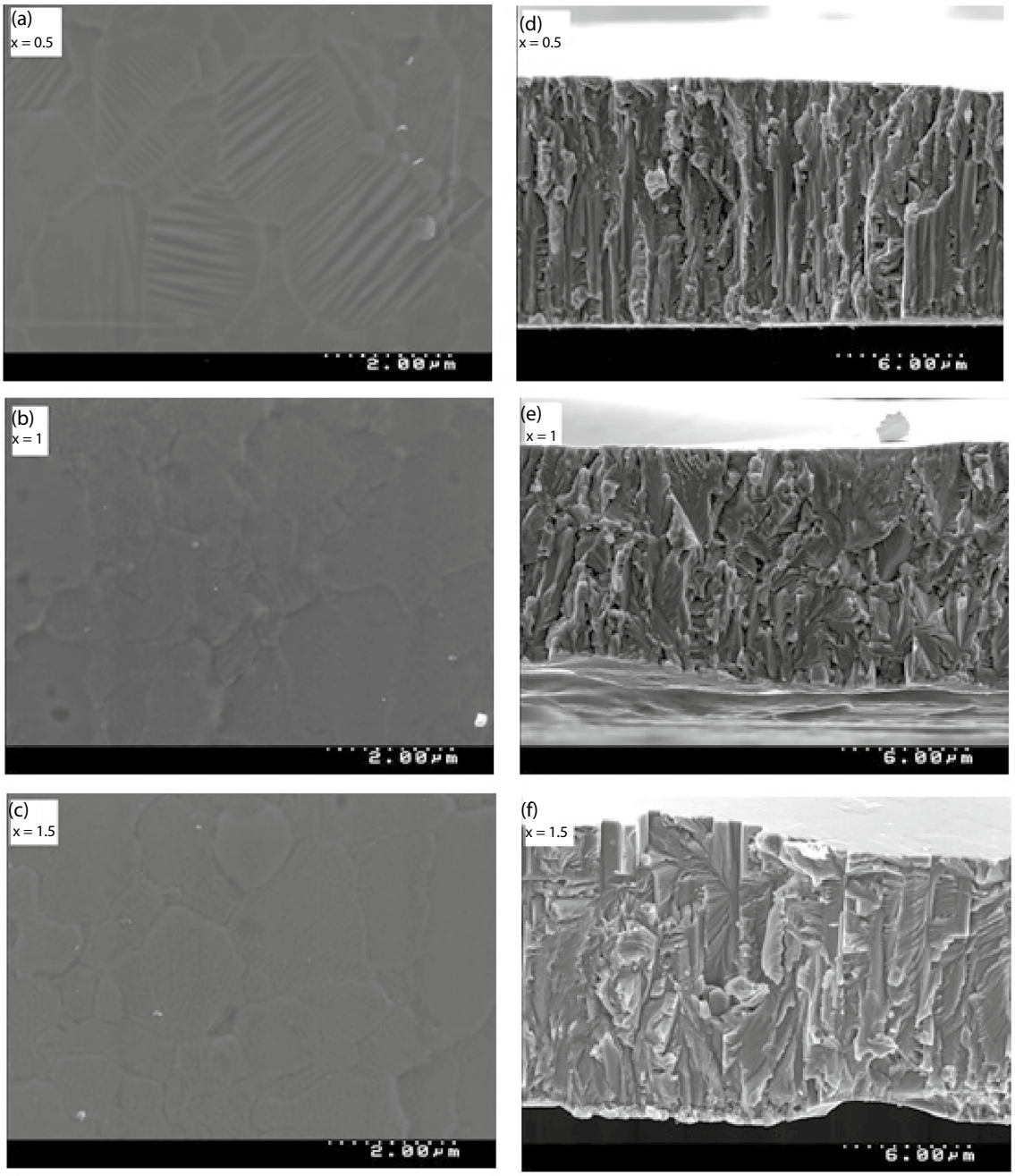

Fig. 1 Typical *SEM* micrographs of the free surface (**a**), (**b**) and (**c**) and fracture cross section (**d**), (**e**) and (**f**) of $Ni_{50-x}Mn_{37}Sn_{13}Fe_x(x = 0.5,\ 1,\ 1.5)$ ribbons

alloys in fig 1 (a) (will be confirmed as the modulated 10*M* structure by *XRD* measurements). On the other hand, the fracture cross section of all ribbons demonstrates a consistent columnar structure oriented perpendicular to the ribbon plane, indicating that heat dissipation during the rapid solidification process induces directional growth of the crystalline phase [37, 38]. The grain sizes and the ribbon thickness were around 2 and 11 μm respectively. The chemical composition of the obtained samples was verified using *EDS* microanalysis, with the results presented in Table 1. As shown, the chemical composition of all the ribbons closely matches the nominal values.

XRD

The *XRD* patterns at room temperature of the obtained ribbons are presented in fig 2. The *XRD* patterns of the $Ni_{50-x}Mn_{37}Sn_{13}Fe_x(1,\ 1.5)$ samples show the presence of

Table 1 Chemical composition of $Ni_{50-x}Mn_{37}Sn_{13}Fe_x (x = 0.5, 1, 1.5)$ ribbons deduced from the *EDS* microanalysis

Alloy	Ni/at%	Mn/at%	Sn/at%	Fe/at%
$x = 0.5$	49.54	36.86	13.20	0.5
$x = 1$	49.07	36.83	13.23	0.98
$x = 1.5$	48.60	36.53	13.40	1.47

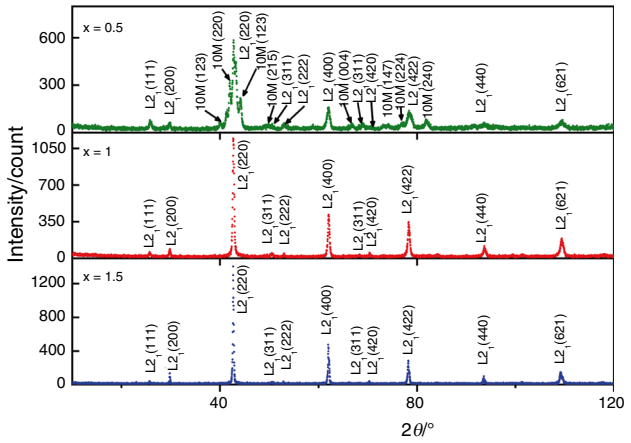

Fig. 2 Room temperature *XRD* patterns of $Ni_{50-x}Mn_{37}Sn_{13}Fe_x (x = 0.5, 1, 1.5)$ ribbons

peaks corresponding to the austenite phase. However, for the $Ni_{50-x}Mn_{37}Sn_{13}Fe_x (x = 0.5)$ composition, in addition to the characteristic peaks of the austenite phase, there are additional peaks that may correspond to the martensitic phase (observed in fig 1 (a)). The *XRD* patterns were refined using the *MAUD* program based on the *Rietveld* analysis. For $Ni_{50-x}Mn_{37}Sn_{13}Fe_x (x = 1, 1.5)$ ribbons, the *Rietveld* refinement was obtained by generating theoretical patterns of the cubic $L2_1$ structure that correspond to the austenite phase. However, for the $Ni_{50-x}Mn_{37}Sn_{13}Fe_x (x = 0.5)$ ribbon, the *Rietveld* refinement was obtained with the cubic $L2_1$ structure and the modulated 10*M* structure, with phase percentages of 80% and 20%, respectively. This indicates the coexistence of the austenite and martensite phases at room temperature in the $Ni_{50-x}Mn_{37}Sn_{13}Fe_x (x = 0.5)$ ribbon (observed in Fig. 1a). The 10*M* modulated martensite is one of the three possible crystallographic structures of the martensite phase, consisting of five cells of the monoclinic $L1_0$ put together with some distortion between the different layers. This martensite structure was also observed in $Ni_{50}Mn_{38}Sb_{12}$ [39], $Ni_{50}Mn_{36}Fe_1In_{13}$ and $Ni_{50}Mn_{35}Fe_2In_{13}$ [40]. The *Rietveld* refinement results presented in Table 2 show a small decrease in the lattice parameter, *a*, of the austenite phase with the increase of Fe concentration. This slight decrease could be attributed to the smaller atomic radius of Fe than that of Ni. A similar lattice shrinkage was reported in Fe-doped Ni-Mn-In melt-spun ribbons [41]. Based on the *XRD* results, it appears that the increase of Fe doping stabilizes the austenite phase at room temperature. The average crystallite size, representing the coherent diffraction domain, also shows notable differences. For the $x = 0.5$ composition, the $L2_1$ phase exhibits a crystallitte size of $113 \pm 2\,nm$, while the 10*M* phase shows a significantly smaller size of $55 \pm 2\,nm$. For the $x = 1$ and $x = 1.5$ compositions, which consist only of the austenite $L2_1$ phase, the crystalline sizes are $142 \pm 3\,nm$ and $139 \pm 2\,nm$, respectively. These values indicate that the crystallite size increases with Fe doping from $x = 0.5$ to $x = 1$, but slightly decreases for $x = 1.5$. The larger crystallite sizes observed for the $x = 1$ and $x = 1.5$ compositions suggest that Fe doping promotes the growth of larger crystallites in these alloys. In contrast, the presence of two phases ($L2_1$ and 10*M*) in the $x = 0.5$ composition results in significantly different crystallite sizes for each phase, with the 10*M* phase showing much smaller crystallites. This disparity in crystalline size can be attributed to the distinct growth mechanisms and stability of the different phases. The nanometric scale of the crystallites observed in these alloys can be attributed to the rapid solidification process inherent in the melt-spinning method used for samples preparation.

DSC

DSC curves, shown in Fig. 3, indicate a first-order reversible martensitic transformation (*MT*) in all samples. The

Table 2 Structural parameters of $Ni_{50-x}Mn_{37}Sn_{13}Fe_x (x = 0.5, 1, 1.5)$ ribbons obtained from the Rietveld refinement of the *XRD* patterns

Alloy	Crystalline structure	Space groupe	Lattice parameters/nm	Crystallite size $< D >$/nm	Goodness of fit (GOF)
$x = 0.5$	$L2_1$ (cubic) (80%)	Fm-3 m	0.5970 ± 0.0004	113 ± 2	1.23
			$a = 0.4038 \pm 0.0006$		
	Modulated 10*M*	*C2/m*	$b = 0.5609 \pm 0.0009$	55 ± 2	
	(monoclinic) (20%)		$c = 2.1478 \pm 0.0008$		
			$\beta = 88.45° \pm 0.07$		
$x = 1$	$L2_1$ (cubic)	Fm-3 m	0.5970 ± 0.0003	142 ± 3	1.18
$x = 1.5$	$L2_1$ (cubic)	Fm-3 m	0.5967 ± 0.0002	139 ± 2	1.37

curves display exothermic and endothermic peaks related to the forward and reverse martensitic transformation, respectively. The start (M_S, A_S) and finish (M_F, A_F) MT characteristic temperatures were determined as the intersection of the tangents of each peak with the baseline. The results are presented in Table 3. M_S was found to decrease with increasing Fe content for all ribbons, M_s values were $329\,K, 255\,K$, and $205\,K$ for $x = 0.5, 1, 1.5$, respectively. The other characteristic transformation temperatures, M_f, A_s, A_f, and the martensitic transformation temperature T_M, defined as $(M_S + A_F)/2$, also shifted toward lower temperatures as the Fe content increased. The decrease in transformation temperatures was most significant in the $Ni_{47}Mn_{37}Sn_{13}Fe_{1.5}$ $(x = 1.5)$ alloy, indicating that Fe strengthens the stability of the cubic austenite parent phase. This behavior has been observed in other Ni-Mn-Sn ferromagnetic alloys and was attributed to the electron valence concentration (e/a), which has a linear correlation with M_s [42]. The addition of Fe atoms reduces the (e/a) due to the lower number of electrons in the outer shell of Fe compared to Ni. This correlation was confirmed by *EDS* microanalysis, which showed that the (e/a) decreased as the Fe content increased (see Table 3). However, other factors such as the Ni/Mn ratio and grain size of the austenitic phase also affect the martensitic transformation and should be taken into account [40, 43]. The thermal hysteresis ΔT, defined as the difference between the temperatures corresponding to exothermic and endothermic peaks, varies between $11\,K$ and $20\,K$, as shown in Table 3. These values are higher than those recently reported for $Ni_{50-x}Fe_xMn_{40}Sn_{10}(x = 0, 2, 4, 6, 8)$, and $Ni_{50}Mn_{36-x}Fe_xSn_{14}(x = 0, 2, 3)$ ribbons [29, 31]. The exothermic and endothermic peaks observed in the *DSC* profiles are utilized to determine the transformation enthalpies (ΔH), by calculating the area between the peaks and the baseline. (ΔH) and the entropy changes (ΔS) associated with the structural transformations are included in Table 3. No trend was observed as a function of the Fe content (or the (e/a) parameter), a similar effect has been reported in Ni-Mn-Sn-Co melt-spun alloys [44]. It is worth noting that while the *XRD* analysis for the $x = 0.5$ alloy suggests the coexistence of austenite and martensite phases at room temperature (80% austenite and 20% martensite), the *DSC* measurements indicate a complete transformation at this temperature. This apparent mismatch could be attributed to several factors. The rapid solidification process during melt spinning can lead to the formation of a metastable state, where the coexistence of phases at room temperature is possible. Additionally, *DSC* measurements may be more sensitive to the transformation process and could detect the complete transformation even if the *XRD* results suggest the presence of a mixture of phases. Further investigation using transmission electron microscopy (*TEM*) could help to clarify this discrepancy and provide a more detailed understanding of the phase distribution in the $x = 0.5$ alloy.

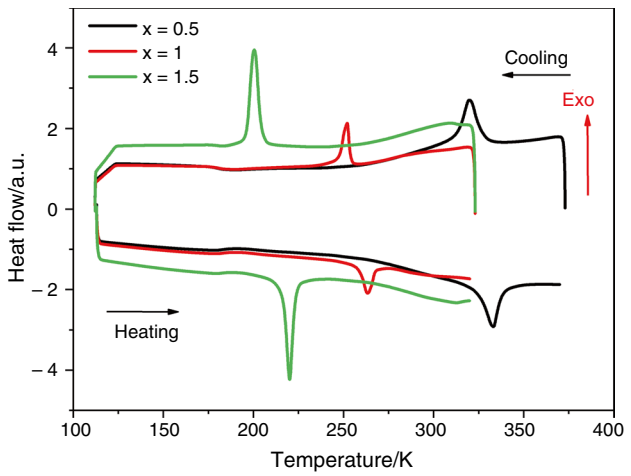

Fig. 3 *DSC* cyclic scans of $Ni_{50-x}Mn_{37}Sn_{13}Fe_x(x = 0.5, 1, 1.5)$ ribbons

Magnetic measurements

M(T) at low applied magnetic field ($H = 50\,Oe$)

Figure 4 illustrates the temperature-dependent behavior of the *ZFC*, *FC*, and *FH* magnetization *M(T)* curves for $Ni_{50-x}Mn_{37}Sn_{13}Fe_x(x = 0.5, 1, 1.5)$ ribbons, measured in the presence of a low magnetic field $(H = 50\,Oe)$. The *ZFC* data for all samples start at low magnetization value that

Table 3 Characteristic transformation temperatures and the electron valence concentration (e/a) of $Ni_{50-x}Mn_{37}Sn_{13}Fe_x(x = 0.5, 1, 1.5)$ ribbons from *DSC* scans and *EDS* microanalysis respectively. (c and h in ΔS stand for cooling and heating respectively)

Alloy	M_s/k	M_f/K	A_s/K	A_f/K	$\Delta T/K$	T_M/K	$\Delta H/Jkg^{-1}$	$\Delta S/Jkg^{-1}K^{-1}$	e/a
$x = 0.5$	329	314	323	338	13	334	34.90(c)	0.11(c)	8,107
							34.40(h)	0,10(h)	
$x = 1$	255	246	258	268	11	255	37.17(c)	0.14(c)	8,096
							38.23(h)	0.15(h)	
$x = 1.5$	205	195	216	224	20	214	21.38(c)	0.10(c)	8,086
							21.70(h)	0.11(h)	

decreases as the Fe concentration increases. For the $x = 0.5$ sample, upon heating, the *ZFC* curve rapidly increases up to about 170 K, after which the magnetization decreases with further heating. Meanwhile, the *FH* and *FC* curves decrease with increasing temperature. At approximately 260 K, the three curves converge, and the magnetization rapidly decreases to zero at around 300 K.

The Curie temperature of the martensitic phase as determined to be $T_C^M = 278\,K$, and no ferromagnetic ordering was observed in the austenitic state of this sample. The structural transformation takes place from a paramagnetic austenitic state to a paramagnetic martensitic state around $M_s = 329\,K$ obtained from calorimetric measurements. For the $x = 1$ sample, *M(T)* increases very slowly up to about 210 K, after which the magnetization begins to increase rapidly until the *ZFC* and *FH* curves merge at about 235 K. Upon further increasing the temperature, *M(T)* first decreases, and an inflection point appears, which corresponds to the Curie temperature T_C^M of the magnetic transition of the martensitic phase $T_C^M = 242\,K$). A sharp increase in magnetization accompanied by splitting between the *FH* and *FC* curves around 250 K up to about 270 K is observed, corresponding to the reverse martensitic transformation from a weak-magnetic martensitic state to a ferromagnetic austenitic state. Further increasing the temperature leads to a decrease in magnetization, and the Curie temperature T_C^A of the austenitic phase for a ferromagnetic to paramagnetic transition is estimated to be $T_C^A = 286\,K$. For the $x = 1.5$ sample, the *ZFC*, *FC*, and *FH* curves start at low magnetization values and increase very slowly upon heating up to the reverse martensitic transformation, which occurs between 195 K and 225 K. The Curie temperature of the austenitic phase for this sample is $T_C^A = 312\,K$. The bifurcation between the *ZFC* and *FC* curves just below T_C^A for this sample could indicate the existence of magnetically inhomogeneous states [5, 8, 45]. The *M(T)* curves for the $x = 1$ and 1.5 samples in Fig. 5 show the existence of a Hopkinson maximum [46] just below the Curie temperature of the austenitic phase, which can be attributed to a decrease in the magnetic anisotropy due to an increase in the magnetic susceptibility below T_C^A. This maximum vanishes with higher magnetic fields (see Fig. 5). The Curie points of the martensitic T_C^M and austenitic T_C^A phases were determined by the minimum of the dM/dT vs. T of *FC* curves, with T_C^A increasing with increasing Fe concentration. The values of the start (M_S^M, A_S^M) and finish (M_F^M, A_F^M) *MT* temperatures, determined by the two-tangent method, the austenitic Curie temperature T_C^A, the martensitic Curie temperature T_C^M, and the magnetization change ΔM between the martensitic and austenitic states of the three alloys deduced from *M(T)* at low applied magnetic field (50 *Oe*) curves are listed in Table 4. The addition of Fe shifts *MT* to lower temperatures (in good agreement with *DSC* scans) and T_C^A to higher temperatures, as evidenced by the results presented in Table 3. This change leads to an enhancement of the magnetic properties of the austenitic phase, resulting in a large jump in magnetization ΔM, which ranges from 3.3 $emu\,g^{-1}$ for $x = 1$ to 17 $emu\,g^{-1}$ for $x = 1.5$, under a low magnetic field of 50 *Oe*. This significant increase in ΔM may improve the magnetocaloric effect of these alloys, and is consistent with previous studies on Ni-Mn-Sn- based Heusler alloys [16, 22, 47–49].

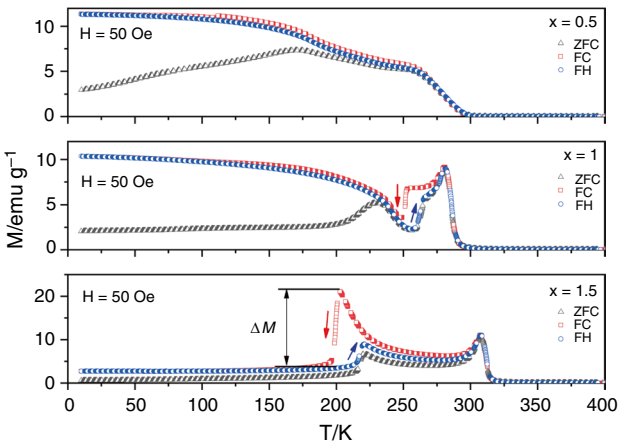

Fig. 4 *ZFC*, *FC* and *FH* magnetization curves *M(T)* measured at low applied magnetic field ($H = 50\,Oe$) for $Ni_{50-x}Mn_{37}Sn_{13}Fe_x (x = 0.5,\ 1,\ 1.5)$ ribbons

M(T) at high applied magnetic field ($H = 50\,k\,Oe$)

Figure 5 represents thermomagnetization curves for $x = 0.5$, 1 and 1.5 compounds at high applied magnetic field ($H = 50\,k\,Oe$). No splitting between *ZFC* and *FC* curves is found, and the Hopkinson maximum vanishes for

Table 4 Characteristic transformation temperatures and magnetization changes of $Ni_{50-x}Mn_{37}Sn_{13}Fe_x (x = 0.5,\ 1,\ 1.5)$ ribbons deduced from the thermomagnetic curves at low applied magnetic field (50 *Oe*)

Alloy	M_s^M/K	M_f^M/K	A_s^M/K	A_f^M/K	T_C^A/K	T_C^M/K	$\Delta M/eum/g$
$x = 0.5$	–	–	–	–	–	278	–
$x = 1$	253	248	256	267	286	242	3.3
$x = 1.5$	203	197	218	222	312	–	17

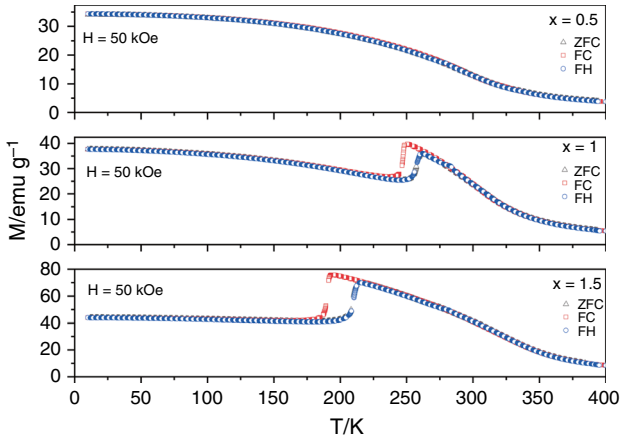

Fig. 5 *ZFC*, *FC* and *FH* magnetization curves *M(T)* measured at high applied magnetic field ($H = 50\,k\,Oe$) for $Ni_{50-x}Mn_{37}Sn_{13}Fe_x(x = 0.5,\ 1,\ 1.5)$ ribbons

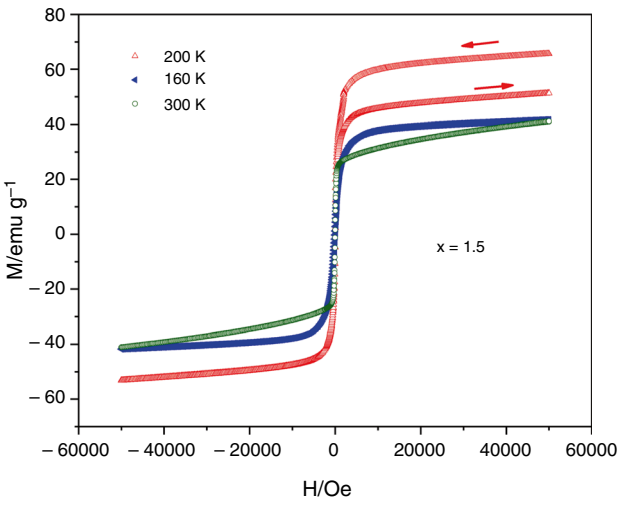

Fig. 6 Isothermal magnetization curves at $300\,K$ (austenite phase), $160\,K$ (just below *MT*) and $200\,K$ (martensitic phase) for $Ni_{50-x}Mn_{37}Sn_{13}Fe_x$ ribbon with $x = 1.5$ showing the metamagnetic-type behavior at $200\,K$

all samples. However, except $x = 0.5$ (no *MT* is observed), a considerable drop in the magnetization of *MT* (ΔM) is seen during cooling, which is related to the weak magnetic martensitic phase. Increasing the applied magnetic field shifts *MT* to lower temperatures and T_C^A to higher temperatures (see Table 5). A large value of the magnetization jump ΔM is observed (from 3.3 *emu* g^{-1} under 50 *Oe* to 14.6 *emu* g^{-1} under 50 *k Oe* for $x = 1$ and from 17 *emu* g^{-1} under 50 *Oe* to 35 *emu* g^{-1} under 50 *k Oe* for $x = 1.5$).

Likewise, the magnetization of both austenitic and martensitic phases is strongly related to the applied magnetic field. Figure 6 shows magnetization as a function of the magnetic field at $300\,K$ (austenitic phase), $160\,K$ (just below *MT*) and $200\,K$ (martensitic phase) for $x = 1.5$. The curve at $300\,K$ represents the behavior of the austenite phase, which is ferromagnetic. The magnetization increases with the applied field and shows a tendency toward saturation. The curve at $160\,K$ represents the behavior of the martensite phase, which is weakly magnetic, and the magnetization remains low even at high magnetic fields. The curve at $200\,K$, just below the martensitic transformation temperature, exhibits a field-induced metamagnetic phase transition. At low fields, the material is in the martensite phase with low magnetization. However, as the field increases, a sudden jump in magnetization occurs at a critical field of approximately $6\,kOe$. This jump corresponds to the field-induced transformation from martensite to austenite. When the field is reduced, the transformation reverses, and the magnetization drops back to the low value, exhibiting hysteresis. This metamagnetic behavior can be attributed to the high ΔM of this compound, resulting in significant Zeeman energy ($\mu_0\,\Delta M\,H$) [15]. The Zeeman energy, which depends on the magnetization and the field strength, acts as a driving force for the transformation. The measurements were performed by incrementally increasing and then decreasing the magnetic field to capture the hysteresis effect. The apparent discontinuity observed in the curves is intrinsic to the metamagnetic phase transition and is consistent with the behavior reported in similar materials [4, 15, 50]. This figure clearly demonstrates the characteristic features of the metamagnetic effect: a sharp magnetization jump at a critical field and hysteresis during the field cycling.

Exchange bias effect

Figure 4 clearly showed a bifurcation between the *ZFC* and *FC* curves for all samples, which corresponds to a magnetic transition in the *ZFC* curves around $250\,K$ for $x = 0.5$ and 1,

Table 5 Characteristic transformation temperatures and magnetization changes of $Ni_{50-x}Mn_{37}Sn_{13}Fe_x(x = 0.5,\ 1,\ 1.5)$ ribbons deduced from the thermomagnetic curves at high applied magnetic field ($50\,k\,Oe$)

Alloy	M_s^M/K	M_f^M/K	A_s^M/K	A_f^M/K	T_C^A/K	T_C^M/K	$\Delta M/eum/g$
$x = 0.5$	–	–	–	–	–	282	–
$x = 1$	247	246	54	258	283	–	14.6
$x = 1.5$	200	187	209	212	284	–	35

and 300 K for $x = 1.5$. We refer to this transition temperature as the conventional exchange bias blocking temperature, T_B. This bifurcation becomes much more pronounced with decreasing temperature, indicating the coexistence of *AFM* and *FM* exchange interaction in the martensitic state [2, 51–53]. To further investigate the exchange bias effect, magnetic hysteresis loops were measured after *FC* ($H = 5\,T$) at various temperatures for all three alloys (Fig. 7). Figure 7(a-c) shows the loops at 10 K, 200 K, 260 K, and 300 K for $x = 0.5$, $x = 1$, and $x = 1.5$, respectively. These loops reveal a clear shift from the origin, particularly at lower temperatures, indicating the presence of exchange bias. The shift, which is attributed to the exchange coupling between ferromagnetic and antiferromagnetic regions, is most pronounced at 10 K and gradually decreases with increasing temperature, consistent with the thermal fluctuations reducing the strength of the exchange coupling. Figure 7(d) compares the hysteresis loops at 10 K for all three alloys, highlighting the increasing exchange bias field with increasing Fe content. This observation further supports the coexistence of antiferromagnetic and ferromagnetic coupling in our samples and confirms that Fe doping enhances the exchange bias effect. Figure 8 presents a double-shifted loop at 10 K after *ZFC* of $x = 1.5$ ribbon (no such behavior is observed for $x = 0.5$ and 1 ribbons), this double-shifted loop, usually observed in certain *EB* materials with *AFM* and *FM* layers [54–59], is another evidence of the existence of *AFM* and *FM* coupling in this sample at low temperatures. A similar behavior was reported in bulk Mn-rich Ni-Mn-Sn Heusler alloys [51]. This explains the lower values of the magnetization observed in the *M(T)* curves of $x = 1.5$ sample at low temperatures. The *ZFC* and *FC* hysteresis loops show a different behavior due to the difference between the magnetic domain structure formed when the system is cooled in the presence of a magnetic field or zero field cooled [51]. Figure 9 shows the variation of the H_{EB} and H_C as function of temperature from 10 K to 300 K for $x = 0.5$, 1 and 1.5 ribbons.

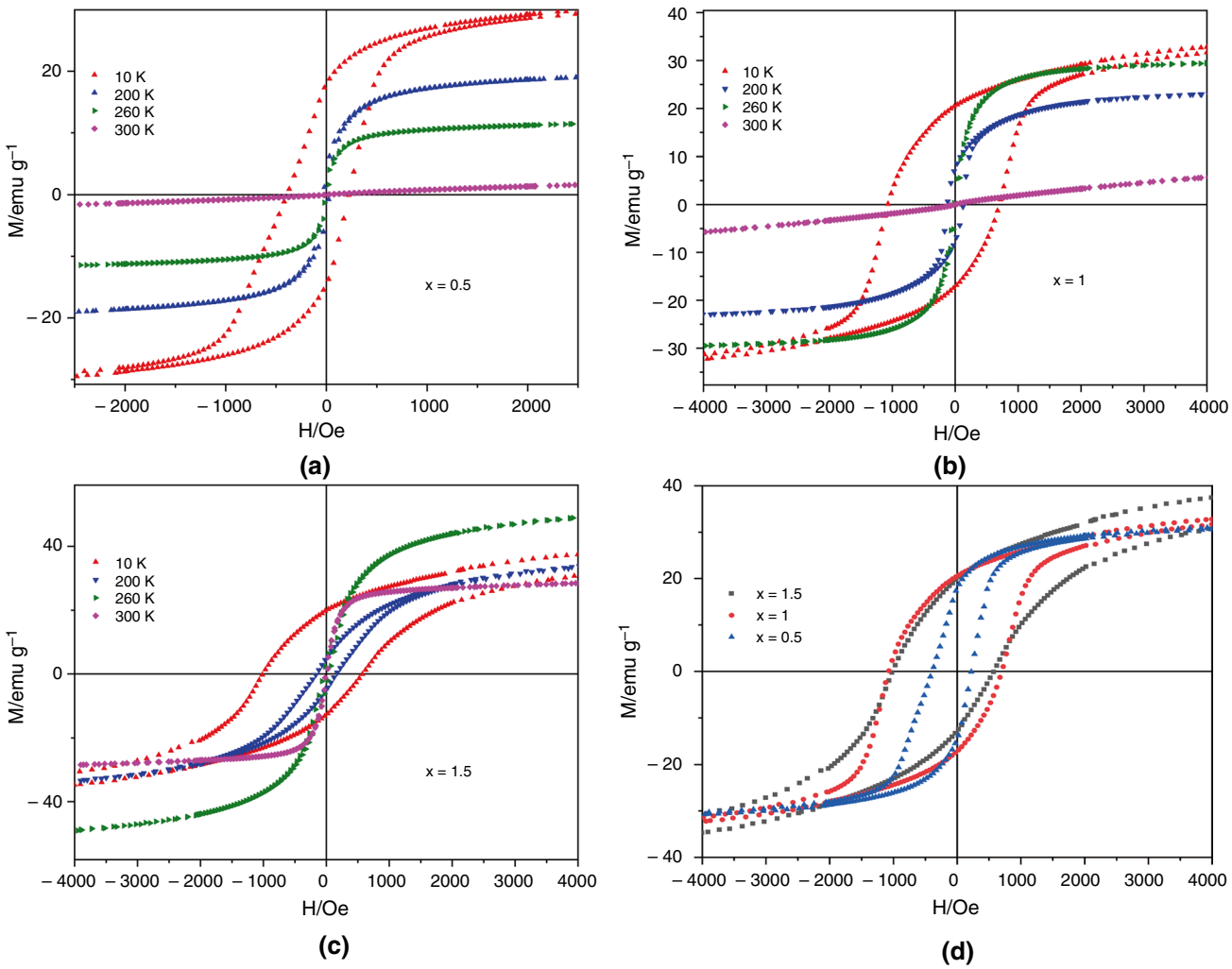

Fig. 7 Magnetic hysteresis loops after *FC* ($H = 5\,T$) at 10 K, 200 K, 260 K, and 300 K:**a** for $x = 0.5$, **b** for $x = 1$ and **c** for $x = 1.5$. **d**: magnetic hysteresis loops after *FC* ($H = 5\,T$) at 10 K for $x = 0.5$, $x = 1$ and $x = 1.5$

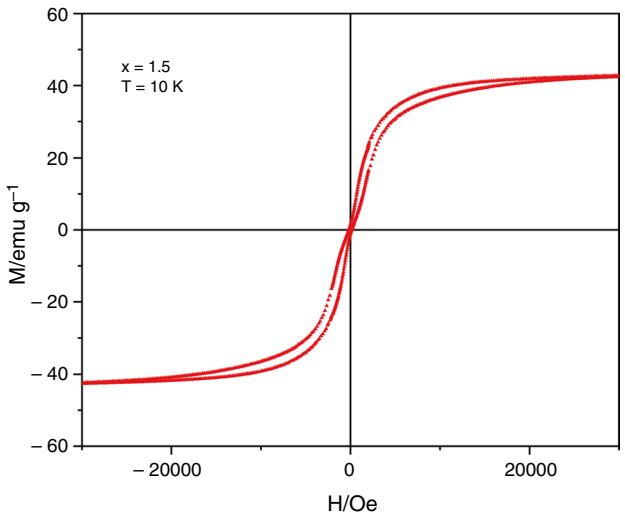

Fig. 8 Double-shifted loop at $10\,K$ after ZFC of $Ni_{50-x}Mn_{37}Sn_{13}Fe_x$ ribbon with $x = 1.5$

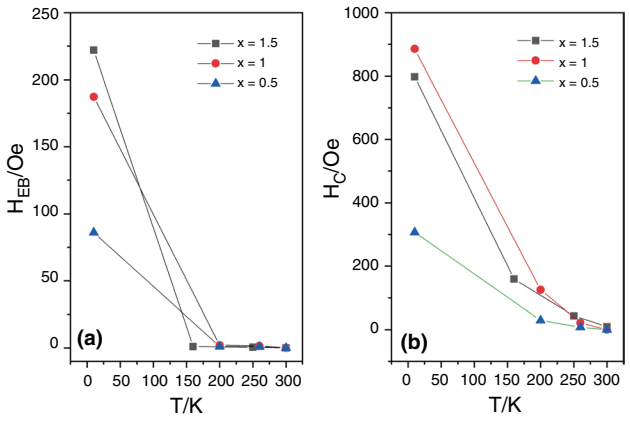

Fig. 9 The variation of the H_{EB} **a** and H_C **b** as function of temperature from $10\,K$ to $300\,K$ for $Ni_{50-x}Mn_{37}Sn_{13}Fe_x(x = 0.5,\ 1,\ 1.5)$ ribbons

Here H_{EB} and H_C are calculated using $H_{EB} = -(H_+ + H_-)/2$ and $H_C = |(H_+ - H_-)|/2$ (H_+ and H_- are the right and left coercive fields, respectively). H_{EB} is found to decrease with increasing temperature for all samples, due to the reduction of the exchange coupling between the *AFM-FM* regions by the thermal fluctuation, and it vanishes at temperatures close to $260\,K$ for $x = 0.5$ and 1, and $300\,K$ for $x = 1.5$. These temperatures corresponding to the exchange bias blocking temperatures are in good agreement with those extracted from thermomagnetization curves. In contrary with several previous reports where a strong peak is observed in H_C near T_B [51–53], in our samples, H_C also shows a monotonic decrease with increasing T. This behavior is consistent with a martensitic phase where nanoscopic *FM* clusters, near the thermal stability, are embedded in a long-range order *AFM* matrix [60, 61].

Conclusions

In the present work, we have investigated the effect of Fe doping on the martensitic transformation and the magnetic properties of $Ni_{50-x}Mn_{37}Sn_{13}Fe_x(x = 0.5,\ 1,\ 1.5)$ magnetic shape memory alloys in the form of ribbons, and the main conclusions can be drawn as follows:

1. At room temperature, x=1 and 1.5 ribbons are $L2_1$-type cubic austenite. However, the $x = 0.5$ ribbon is a mixture of cubic $L2_1$ and the modulated $10M$ structure indicating the coexistance of austenite and martensite phases.
2. The addition of Fe shifts the martensitic transformation to lower temperatures and the Curie point of the austenitic phase T_C^A to higher temperatures which leads to the enhancement of the magnetism of the austenitic phase.
3. A large value of the magnetization jump, ΔM, is detected (from $3.3\,emu\,g^{-1}$ for $x = 1$ to $17\,emu\,g^{-1}$ for $x = 1.5$ under $50\,Oe$ applied magnetic field).
4. Exchange-bias effect was found in all ribbons, which confirms the coexistence of antiferromagnetic and ferromagnetic coupling in our samples. The exchange bias effect is found to increase with the increase in Fe content.

Funding Open Access funding provided thanks to the CRUE-CSIC agreement with Springer Nature.

References

1. Pathak AK, Khan M, Gautam BR, Stadler S, Dubenko I, Ali N. Exchange bias in bulk Ni-Mn-In-based heusler alloys. J Magn Magn Mater. 2009;321(8):963–5. https://doi.org/10.1016/j.jmmm.2008.03.008.
2. Nayak AK, Suresh K, Nigam A. Observation of enhanced exchange bias behavior in NiCoMnSb heusler alloys. J Phys D Appl Phys. 2009;42(11): 115004. https://doi.org/10.1088/0022-3727/42/11/115004.
3. Wang B, Liu Y, Ren P, Xia B, Ruan K, Yi J, Ding J, Li X, Wang L. Large exchange bias after zero-field cooling from an unmagnetized state. Phys Rev Lett. 2011;106(7): 077203. https://doi.org/10.1103/PhysRevLett.106.077203.

4. Kainuma R, Imano Y, Ito W, Sutou Y, Morito H, Okamoto S, Kitakami O, Oikawa K, Fujita A, Kanomata T. Magnetic-field-induced shape recovery by reverse phase transformation. Nature. 2006;439(7079):957–60. https://doi.org/10.1038/nature04493.
5. Krenke T, Duman E, Acet M, Wassermann EF, Moya X, Mañosa L, Planes A. Inverse magnetocaloric effect in ferromagnetic Ni-Mn-Sn alloys. Nat Mater. 2005;4(6):450–4. https://doi.org/10.1038/nmat1395.
6. Liu J, Gottschall T, Skokov KP, Moore JD, Gutfleisch O. Giant magnetocaloric effect driven by structural transitions. Nat Mater. 2012;11(7):620–6. https://doi.org/10.1038/nmat3334.
7. Yu S, Ma L, Liu G, Liu Z, Chen J, Cao Z, Wu G, Zhang B, Zhang X. Magnetic field-induced martensitic transformation and large magnetoresistance in NiCoMnSb alloys. Appl Phys Lett. 2007;90(24): 242501. https://doi.org/10.1063/1.2748095.
8. Koyama K, Okada H, Watanabe K, Kanomata T, Kainuma R, Ito W, Oikawa K, Ishida K. Observation of large magnetoresistance of magnetic heusler alloy $Ni_{50}Mn_{36}Sn_{14}$ in high magnetic fields. Appl Phys Lett. 2006;89(18): 182510. https://doi.org/10.1063/1.2374868.
9. Yang Z, Cong D, Huang L, Nie Z, Sun X, Zhang Q, Wang Y. Large elastocaloric effect in a Ni-Co-Mn-Sn magnetic shape memory alloy. Mater Des. 2016;92:932–6. https://doi.org/10.1016/j.matdes.2015.12.118.
10. Irzhak A, Zakharov D, Kalashnikov V, Koledov V, Kuchin D, Lebedev G, Lega P, Perov E, Pikhtin N, Pushin V. Actuators based on composite material with shape-memory effect. J Commun Technol Electron. 2010;55:818–30. https://doi.org/10.1134/S1064226910070120.
11. Zakharov D, Lebedev G, Irzhak A, Afonina V, Mashirov A, Kalashnikov V, Koledov V, Shelyakov A, Podgorny D, Tabachkova N. Submicron-sized actuators based on enhanced shape memory composite material fabricated by FIB-CVD. Smart Mater Struct. 2012;21(5): 052001. https://doi.org/10.1088/0964-1726/21/5/052001.
12. Enkovaara J, Ayuela A, Nordström L, Nieminen RM. Structural, thermal, and magnetic properties of Ni_2MnGa. J Appl Phys. 2002;91(10):7798–800. https://doi.org/10.1063/1.1453933.
13. Lázpita P, Barandiarán J, Gutiérrez J, Feuchtwanger J, Chernenko V, Richard M. Magnetic moment and chemical order in off-stoichiometric NiMnGa ferromagnetic shape memory alloys. New J Phys. 2011;13(3): 033039. https://doi.org/10.1088/1367-2630/13/3/033039.
14. Wang W, Yu J, Zhai Q, Luo Z, Zheng H. Co-doping effect on the martensitic transformation and magnetic properties of $Ni_{49}Mn_{39}Sn_{12}$ alloy. J Magn Magn Mater. 2013;346:103–6. https://doi.org/10.1016/j.jmmm.2013.07.025.
15. Lázpita P, Sasmaz M, Barandiarán J, Chernenko V. Effect of Fe doping and magnetic field on martensitic transformation of Mn-Ni(Fe)-Sn metamagnetic shape memory alloys. Acta Mater. 2018;155:95–103. https://doi.org/10.1016/j.actamat.2018.05.052.
16. Krenke T, Duman E, Acet M, Moya X, Mañosa L, Planes A. Effect of Co and Fe on the inverse magnetocaloric properties of Ni-Mn-Sn. J Appl Phys. 2007;102(3): 033903.
17. Kock I, Edler T, Mayr SG. Growth behavior and intrinsic properties of vapor-deposited iron palladium thin films. J Appl Phys. 2008;103(4): 046108.
18. Wójcik A, Maziarz W, Szczerba MJ, Sikora M, Dutkiewicz J, Cesari E. Tuning magneto-structural properties of $Ni_{44}Co_6Mn_{39}Sn_{11}$ heusler alloy ribbons by Fe-doping. Mater Sci Eng: B. 2016;209:23–9. https://doi.org/10.1016/j.mseb.2016.03.002.
19. Li H, Fang Y, Feng S, Zhai Q, Luo Z, Zheng H. Magnetostructural transition behavior in Fe-doped heusler Mn-Ni-In ribbon materials. J Magn Magn Mater. 2016;417:267–71. https://doi.org/10.1016/j.jmmm.2016.05.087.
20. Ghosh A, Mandal K. Effect of Fe substitution on the magnetic and magnetocaloric properties of Mn-rich Mn-Ni-Fe-Sn off-stoichiometric heusler alloys. J Appl Phys. 2015;117(9):093909. https://doi.org/10.1063/1.4913951.
21. Zhang H, Zhang X, Qian M, Yuan B, Geng L. Effect of partial metamagnetic and magnetic transition coupling on the magnetocaloric effect of Ni-Mn-Sn-Fe alloy. Intermetallics. 2019;105:124–9. https://doi.org/10.1016/j.intermet.2018.11.014.
22. Zhang H, Qian M, Zhang X, Wei L, Cao F, Xing D, Cui X, Sun J, Geng L. Martensite transformation and magnetic properties of Fe-doped Ni-Mn-Sn alloys with dual phases. J Alloys Compounds. 2016;689:481–8. https://doi.org/10.1016/j.jallcom.2016.07.282.
23. Sasmaz M, Chernenko V, Martinez E, Lázpita P, Barandiarán J, Gutiérrez J, Aydogdu Y. Structure and magnetic-field induced effects in Mn-Ni(Fe)-Sn metamagnetic shape memory alloys. Mater Today: Proceedings. 2015;2:849–52. https://doi.org/10.1016/j.matpr.2015.07.415.
24. Zhang H, Qian M, Zhang X, Jiang S, Wei L, Xing D, Sun J, Geng L. Magnetocaloric effect of Ni-Fe-Mn-Sn microwires prepared by melt-extraction technique. Materials. 2017. https://doi.org/10.1016/j.matdes.2016.10.077.
25. Wu Z, Liu Z, Yang H, Liu Y, Wu G, Woodward RC. Metallurgical origin of the effect of Fe doping on the martensitic and magnetic transformation behaviors of $Ni_{50}Mn_{40-x}Sn_{10}Fe_x$ magnetic shape memory alloys. Intermetallics. 2011;19(4):445–52. https://doi.org/10.1016/j.intermet.2010.10.010.
26. Das R, Sarma S, Perumal A, Srinivasan A. Effect of Co and Cu substitution on the magnetic entropy change in $Ni_{46}Mn_{43}Sn_{11}$ alloy. J Appl Phys. 2011. https://doi.org/10.1063/1.3540327.
27. Bruno NM, Yegin C, Karaman I, Chen J-H, Ross JH Jr, Liu J, Li J. The effect of heat treatments on $Ni_{43}Mn_{42}Co_4Sn_{11}$ meta-magnetic shape memory alloys for magnetic refrigeration. Acta Mater. 2014;74:66–84. https://doi.org/10.1016/j.actamat.2014.03.020.
28. Khovaylo VV, Rodionova VV, Shevyrtalov SN, Novosad V. Magnetocaloric effect in "reduced'' dimensions: Thin films, ribbons, and microwires of heusler alloys and related compounds. Phys Status Solidi (b). 2014;251(10):2104–13. https://doi.org/10.1002/pssb.201451217.
29. Deltell A, Mohamed AE-MA, Álvarez-Alonso P, Ipatov M, Andrés J, Gonzalez JA, Sánchez T, Zhukov A, Escoda M, Suñol J. Martensitic transformation, magnetic and magnetocaloric properties of Ni-Mn-Fe-Sn heusler ribbons. J Market Res. 2021;12:1091–103. https://doi.org/10.1016/j.jmrt.2021.03.049.
30. Xing C, Zhang H, Long K, Xiao Y, Zhang H, Qiu Z, He D, Liu X, Zhang Y, Long Y. The effect of different atomic substitution at Mn site on magnetocaloric effect in $Ni_{50}Mn_{35}Co_2Sn_{13}$ alloy. Curr Comput-Aided Drug Des. 2018;8(8):329. https://doi.org/10.3390/cryst8080329.
31. Aguilar-Ortiz CO, Soto-Parra D, Álvarez-Alonso P, Lázpita P, Salazar D, Castillo-Villa PO, Flores-Zúñiga H, Chernenko V. Influence of Fe doping and magnetic field on martensitic transition in Ni-Mn-Sn melt-spun ribbons. Acta Mater. 2016;107:9–16. https://doi.org/10.1016/j.actamat.2016.01.041.
32. Dadda K, Alleg S, Souilah S, Suñol J, Dhahri E, Bessais L, Hlil E. Critical behavior, magnetic and magnetocaloric properties of melt-spun $Ni_{50}Mn_{35}Sn_{15}$ ribbons. J Alloys Compounds. 2018;735:1662–72. https://doi.org/10.1016/j.jallcom.2017.11.277.
33. Yuhasz WM, Schlagel DL, Xing Q, Dennis KW, McCallum RW, Lograsso T. Influence of annealing and phase decomposition on the magnetostructural transitions in $Ni_{50}Mn_{39}Sn_{11}$. J Appl Phys. 2009. https://doi.org/10.1063/1.3067855.

34. Ma S, Shih C, Liu J, Yuan J, Lee S, Lee Y, Chang H, Chang W. Wheel speed-dependent martensitic transformation and magnetocaloric effect in Ni-Co-Mn-Sn ferromagnetic shape memory alloy ribbons. Acta Mater. 2015;90:292–302. https://doi.org/10.1016/j.actamat.2015.03.011.
35. Lutterotti L. Maud: a rietveld analysis program designed for the internet and experiment integration. Acta Crystallogr A. 2000;56(s1):54. https://doi.org/10.1107/S0108767300021942.
36. Rietveld HM. A profile refinement method for nuclear and magnetic structures. J Appl Crystallogr. 1969;2(2):65–71. https://doi.org/10.1107/s0021889869006558.
37. Sánchez Llamazares JL, Sanchez T, Santos J, Pérez M, Sanchez M, Hernando B, Escoda L, Suñol J, Varga R. Martensitic phase transformation in rapidly solidified $Mn_{50}Ni_{40}In_{10}$ alloy ribbons. Appl Phys Lett. 2008. https://doi.org/10.1063/1.2827179.
38. Hernando B, Llamazares J, Santos J, Escoda L, Suñol J, Varga R, Baldomir D, Serantes D. Thermal and magnetic field-induced martensite-austenite transition in $Ni_{50.3}Mn_{35.3}Sn_{14.4}$ ribbons. Appl Phys Lett. 2008. https://doi.org/10.1063/1.2838356.
39. Khan M, Ali N, Stadler S. Inverse magnetocaloric effect in ferromagnetic $Ni_{50}Mn_{37+x}Sb_{13-x}$ heusler alloys. J Appl Phys. 2007. https://doi.org/10.1063/1.2710779.
40. Jing C, Wang X, Liao P, Li Z, Yang Y, Kang B, Deng D, Cao S, Zhang J, Zhu J. Martensitic phase transition, inverse magnetocaloric effect, and magnetostrain in $Ni_{50}Mn_{37-x}Fe_xIn_{13}$ heusler alloys. J Appl Phys. 2013. https://doi.org/10.1063/1.4818486.
41. Rao NR, Muthu SE, Arumugam S, Raja MM, Suresh KG. Effect of Fe on the martensitic transition, magnetic and magnetocaloric properties in ni-mn-In melt-spun ribbons. Defence Sci J. 2016;66(4):403–12.
42. Krenke T, Moya X, Aksoy S, Acet M, Entel P, Mañosa L, Planes A, Elerman Y, Yücel A, Wassermann E. Electronic aspects of the martensitic transition in Ni-Mn based heusler alloys. J Magn Magn Mater. 2007;310(2):2788–9. https://doi.org/10.1016/j.jmmm.2006.10.1139.
43. Yin M, Nash P. The effect of a fourth element (Co, Cu, Fe, Pd) on the standard enthalpy of formation of the heusler compound Ni_2MnSn. J Alloys Compounds. 2016;667:184–90.
44. Deltell A, Escoda L, Saurina J, Suñol JJ. Martensitic transformation in Ni-Mn-Sn-Co heusler alloys. Metals. 2015;5(2):695–705. https://doi.org/10.3390/met5020695.
45. Santos J, Sanchez T, Alvarez P, Sanchez M, Sánchez Llamazares JL, Hernando B, Escoda L, Suñol J, Varga R. Microstructure and magnetic properties of $Ni_{50}Mn_{37}Sn_{13}$ heusler alloy ribbons. J Appl Phys. 2008. https://doi.org/10.1063/1.2832330.
46. Hopkinson J. Magnetic properties of alloys of nickel and iron. Proc R Soc Lond. 1890;47(286–291):23–4. https://doi.org/10.1098/rspl.1890.0001.
47. Krenke T, Acet M, Wassermann EF, Moya X, Mañosa L, Planes A. Ferromagnetism in the austenitic and martensitic states of Ni-Mn-In alloys. Phys Rev B. 2006;73(17): 174413. https://doi.org/10.1103/PhysRevB.73.174413.
48. Passamani E, Córdova C, Alves A, Moscon P, Larica C, Takeuchi A, Biondo A. Magnetic studies of Fe-doped martensitic $Ni_2Mn_{1.44}Sn_{0.56}$-type heusler alloy. J Phys D: Appl Phys. 2009;42(21): 215006. https://doi.org/10.1088/0022-3727/42/21/215006.
49. Zhang Y, Zhang L, Zheng Q, Zheng X, Li M, Du J, Yan A. Enhanced magnetic refrigeration properties in mn-rich Ni-Mn-Sn ribbons by optimal annealing. Sci Rep. 2015;5(1):11010. https://doi.org/10.1038/srep11010.
50. Sarkar SK, Babu PD, Sharma VK, Kaushik SD, Goswami S, Manekar MA. 2024 Enhanced metamagnetic shape memory effect in Heusler-type Ni37Co11Mn43Sn9 polycrystalline ferromagnetic shape memory alloy. Acta Materialia. 276:120126.https://doi.org/10.48550/arXiv.2402.18992
51. Khan M, Dubenko I, Stadler S, Ali N. Exchange bias in bulk Mn-rich Ni-Mn-Sn Heusler alloys. J Appl Phys. 2007. https://doi.org/10.1063/1.2818016.
52. Wang B, Liu Y, Wang L, Huang S, Zhao Y, Yang Y, Zhang H. Exchange bias and its training effect in the martensitic state of bulk polycrystalline $Ni_{49.5}Mn_{34.5}In_{16}$. J Appl Phys. 2008. https://doi.org/10.1063/1.2973187.
53. Xuan H, Cao Q, Zhang C, Ma S, Chen S, Wang D, Du Y. Large exchange bias field in the Ni-Mn-Sn heusler alloys with high content of Mn. Appl Phys Lett. 2010. https://doi.org/10.1063/1.3428782.
54. Chien C, Gornakov V, Nikitenko V, Shapiro A, Shull R. Hybrid domain walls and antiferromagnetic domains in exchange-coupled ferromagnet/antiferromagnet bilayers. Phys Rev B. 2003;68(1): 014418. https://doi.org/10.1103/PhysRevB.68.014418.
55. Lai C-H, Wang Y-H, Chang C-R, Yang J-S, Yao Y. Exchange-bias-induced double-shifted magnetization curves in Co biaxial films. Phys Rev B. 2001;64(9): 094420. https://doi.org/10.1103/PhysRevB.64.094420.
56. Zhao H-W, Wang W, Wang Y, Zhan W, Xiao J. Investigation of exchange bias in FeMnC/FeMn bilayers. J Appl Phys. 2002;91(10):6893–5. https://doi.org/10.1063/1.1447186.
57. Gökemeijer N, Cai J, Chien C. Memory effects of exchange coupling in ferromagnet/antiferromagnet bilayers. Phys Rev B. 1999;60(5):3033. https://doi.org/10.1103/PhysRevB.60.3033.
58. Miltényi P, Gierlings M, Bamming M, May U, Güntherodt G, Nogués J, Gruyters M, Leighton C, Schuller IK. Tuning exchange bias. Appl Phys Lett. 1999;75(15):2304–6. https://doi.org/10.1063/1.124998.
59. Brück S, Sort J, Baltz V, Surinach S, Munoz JS, Dieny B, Baró MD, Nogues J. Exploiting length scales of exchange-bias systems to fully tailor double-shifted hysteresis loops. Adv Mater. 2005;17(24):2978–83. https://doi.org/10.1002/adma.200500544.
60. Bhatti KP, El-Khatib S, Srivastava V, James R, Leighton C. Small-angle neutron scattering study of magnetic ordering and inhomogeneity across the martensitic phase transformation in $Ni_{50-x}Co_xMn_{40}Sn_{10}$ alloys. Phys Rev B. 2012;85(13): 134450. https://doi.org/10.1103/PhysRevB.85.134450.
61. Zhukov A. Novel Functional Magnetic Materials. Springer, Switzerland 2016; https://doi.org/10.1007/978-3-319-26106-5